JOURNAL OF GEOPHYSICAL RESEARCH, VOL. 95, NO. A5, PAGES 6505–6517, MAY 1, 1990

VLF Wave Emissions by Pulsed and DC Electron Beams in Space 2. Analysis of Spacelab 2 Results

G. D. REEVES,[1] P. M. BANKS, T. NEUBERT, AND K. J. HARKER

Telecommunications and Radioscience Laboratory, Stanford University, Stanford, California

D. A. GURNETT

Department of Physics and Astronomy, University of Iowa, Iowa City

Experiments investigating the generation of radio frequency waves in space plasmas by the injection of artificial electron beams into ionospheric plasmas were conducted in July and August of 1985 on the Spacelab 2 space shuttle mission. Among the results were the production of broadband electromagnetic emissions from continuous and square-wave-modulated, low-power (1-keV, 50/100-mA) electron beams and the observation of narrow-band radiation from pulsed beam operations. Observations from the Spacelab 2 experiments were presented by Reeves et al. (1988*b*). This paper is a sequel to that earlier work and presents analysis of the observations. Observations of narrow-band radiation are compared with the predictions of a theory of wave generation by pulsed electron beams (Harker and Banks, 1987). Good agreement between observations and predictions is found for the $s = 0$, root 2 solutions which represent Cherenkov radiation with wave normal angles less than the Gendrin angle. For the broadband emissions, predictions using a single-ion, cold plasma theory are compared with the general features observed in the data. Broadband emissions from dc and pulsed electron beams also have features which can be understood in terms of the characteristics of whistler mode waves which are produced by the Cherenkov resonance. All observations were made within the near field of waves in this mode. Waves observed outside the predicted region of propagation are identified as near-field components. Study of wave amplitudes in a coordinate system defined by the orbiter velocity vector indicates the presence of a wake structure behind the beam. Large-amplitude waves observed in the beam and beam-wake regions may include additional, electrostatic contributions to the wave fields. The relative contributions of electromagnetic and electrostatic fields are discussed, and an order of magnitude estimate of the Poynting flux is presented.

1. INSTRUMENTATION

The Spacelab 2 electron beam experiments were part of a continuing effort to investigate the properties of beam-plasma-wave interactions using active experiments in space. Summaries of previous research with electron beams in space can be found in the work by *Reeves et al.* [1988*b*], *Winckler* [1980], and *Myers et al.* [1989]. The analysis presented here is based on the observations from a low-frequency wideband wave receiver. The data were obtained by cooperative use of the instruments in the Stanford University/Utah State University vehicle charging and potential (VCAP) experiment [*Banks et al.*, 1987, *Hawkins*, 1988] and the University of Iowa plasma diagnostics package (PDP) [*Shawhan et al.*, 1984*a*]. The VCAP experiment included a fast pulsed electron generator (FPEG) which produced a 1-keV electron beam with currents of 50 or 100 mA. The beam was operated both continuously, in dc mode, and in pulsed mode with frequencies and duty cycles which were command controlled. The VCAP experiment package also included a spherical retarding and potential analyzer, a Langmuir probe, and charge and current probes which were used to investigate vehicle charging and the collection of return current during electron beam operations. More information on the VCAP instruments and their use on the Spacelab 2 and STS 3/OSS 1 missions can be found in the work by *Hawkins* [1988] and *Reeves et al.* [1988*a*].

The waves produced by the injection of electrons into the ambient plasma were measured using instruments on the PDP. The PDP contained a variety of instruments for the investigation of the ambient plasma and wave environment around the orbiter and the modifications to that environment produced by electron beam injection. The PDP was operated both when it was mounted in the orbiter payload bay and when it was released as a free-flying satellite out to distances of several hundred meters from the orbiter. During the 6-hour free flight, the PDP was spin stabilized with a rotation period of $\sim$ 13 s. The PDP instruments included a wideband wave receiver and several arrays of band-pass filters. These instruments were used to investigate the wave fields produced by the interaction of the electron beam with the ionospheric plasma. The wideband receiver recorded signals in the range 0–30 kHz using a 1-kHz-wide channel (the ELF channel) which monitored the 0–1 kHz frequency range and a 10-kHz-wide channel (the VLF channel) which was switched between the frequency ranges 0–10, 10–20, and 20–30 kHz. Both channels of the wideband receiver were connected, alternately, to an electric dipole antenna or a magnetic search coil antenna. The total output signal strength was kept within strict limits by the action of an automatic gain control (AGC). The PDP filter banks included the IMP/Helios instrument, an array of 16 filters with 10% bandwidths in the frequency range 31 Hz to 178 kHz, and a medium frequency receiver (MFR) which was used to probe

[1] Now at Earth and Space Science Division, Los Alamos National Laboratory, Los Alamos, New Mexico.

Paper number 89JA02858.
0148-0227/90/89JA-02858$05.00

the ac electric fields using eight filters in the frequency range 316 kHz to 17.8 MHz. Filter bank data could be used to observe the general structure of electric fields produced by beam operations in the format of a continuous time record (1.6-s time steps) without the complications of automatic gain control or the antenna and frequency switching used in the wideband receiver measurements. Observations of wave fields produced by electron beam operations on Spacelab 2 using the wideband receiver have been reported by *Bush et al.* [1987], *Reeves et al.* [1988*b*], and *Neubert et al.* [1989*a*]. Observations using the IMP/Helios and MFR instruments of funnel-shaped wave emissions resulting from Cherenkov, resonance cone propagation of radiation from electron beams have been discussed by *Gurnett et al.* [1986] and *Farrell et al.* [1988]. (These two papers will hereafter be referred to as "*GF*.") More detailed descriptions of the instruments on the PDP and the use of those instruments for the investigation of the plasma and wave environment in the vicinity of the orbiter can be found in the work by *Shawhan et al.* [1984*b*], *Gurnett et al.* [1986], and *Farrell et al.* [1988].

2. A Summary of Spacelab 2 Wave Observations

The analysis presented here is based on the observations and discussion presented by *Reeves et al.* [1988*b*] which are summarized in this section. In that paper (which will be referred to as "*RBN*") the amplitudes, spectral characteristics, and time evolution of waves generated by continuous and modulated electron beams were considered. Results were presented from three separate electron beam wave generation sequences on Spacelab 2. These sequences are referred to as the "DC flux tube connection," the "Pulsed flux tube connection," and the "Prox Ops" sequences. In the flux tube connection sequences the PDP was operated as a free-flying subsatellite, and the orbiter maneuvered such that the orbiter and the PDP lay on the same geomagnetic field line: the so-called "conjunction field line." Figure 1 shows the perpendicular distance from the PDP to the conjunction field line for the DC and Pulsed flux tube connection sequences. At the times of closest approach the PDP was ~ 200 m from the orbiter along the direction of the geomagnetic field. The trajectories during these sequences are seen to be quite similar, but during the DC flux tube connection sequence the FPEG was operated continuously with a current of 50 mA while during the Pulsed flux tube connection sequence the FPEG was square-wave modulated at 1.22 kHz with a 50% duty cycle and a 100-mA current. Both the dc and pulsed modes inject the same average amount of power, and it was found that both produce broadband waves with comparable amplitude when measured at similar distances with respect to the conjunction field line (*RBN*).

Pulsed electron beams were found to produce narrow-band emissions at the pulsing frequency and harmonics of that frequency which are superimposed upon the broadband spectrum. During the Pulsed flux tube connection it was found that there was a constant ratio of the amplitude of narrow-band emissions at the pulsing frequency (1.22 kHz, 12-Hz bandwidth) to the amplitude of broadband emissions near that frequency (1.7–1.8 kHz, average over 12-Hz components). For the electric field measurements the narrow-band emissions were approximately 5 times stronger

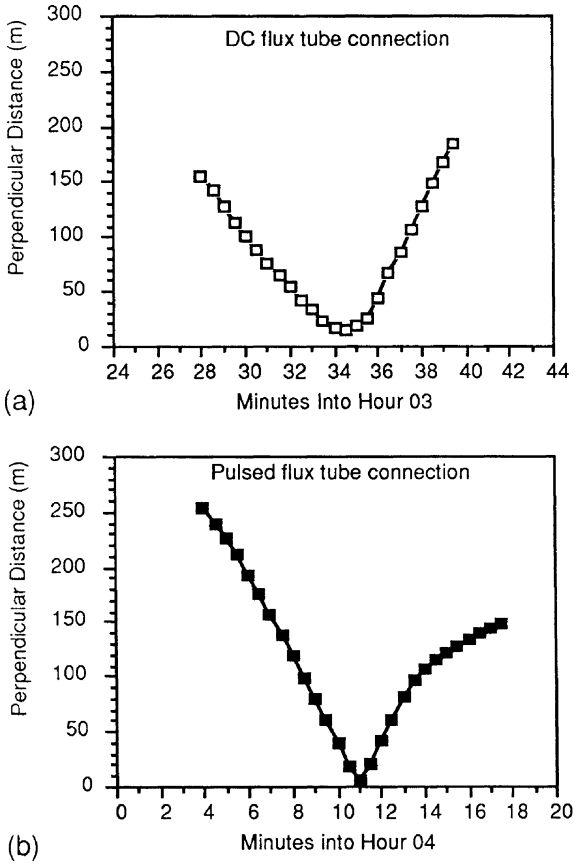

Fig. 1. The location of the PDP in the orbiter reference frame. The origin of this frame is the nose of the orbiter. Perpendicular distances were calculated based on the direction of the geomagnetic field. (*a*) For the DC flux tube connection the time of closest approach of the PDP to a field line passing through the FPEG was estimated to be 0334:10 UT. (*b*) For the Pulsed flux tube connection the FPEG was turned on at 0411:13 UT, which was near the time of closest approach.

than the broadband emissions. For the magnetic field measurements the narrow-band emissions were about 15 times stronger. These results were independent of where the fields were measured (*RBN*). (Amplitudes from the wideband receiver data presented here and in *RBN* are the amplitudes of the 12-Hz Fourier components used in the analysis of the digitized data for both broadband and narrow-band emissions.)

Broadband Wave Observations

Definition of Three Wave Amplitude Zones. High time and frequency resolution data were obtained with the PDP wideband wave receiver instrument. Because the PDP was moving across the conjunction field line during the flux tube connection sequences, the spectra, which provide wave amplitude as a function of frequency and time, can also be interpreted in terms of amplitude as a function of frequency and distance from the beam.

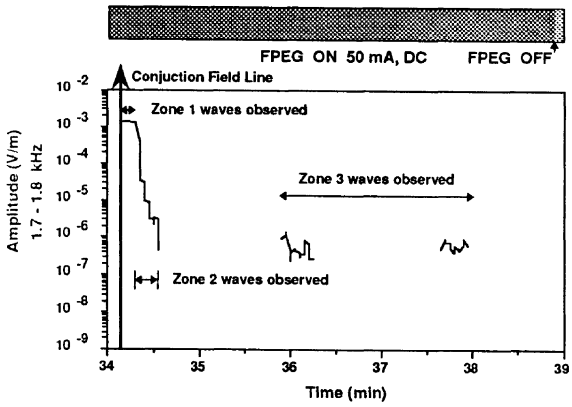

Fig. 2. The three zones of wave amplitude as observed during the DC flux tube connection are shown. Electric field amplitudes in the frequency range 1.7-1.8 kHz are plotted as a function of time while the PDP moves further from the beam. Zone 1 is observed closest to the beam, and wave amplitudes saturate the wideband receiver. Zone 2 is characterized by rapid decrease in amplitude with distance. Zone 3 is characterized by slow decrease in amplitude with distance. Gaps in the data are due to the antenna switching pattern.

The amplitudes of broadband and narrow-band, electric and magnetic wave fields were found, by *RBN*, to vary with both frequency and perpendicular distance to the beam. The spatial regions in which broadband waves of different amplitudes were observed were defined, in *RBN*, in terms of three zones. The three zones of wave amplitude are illustrated in Figure 2. Figure 2 shows some of the same data as Figure 6 of *RBN*. The beam is on in dc mode , and the PDP is moving further from the beam during this interval. The amplitudes are for the frequencies 1.7–1.8 kHz and were measured with the VLF wideband receiver. The amplitudes were derived using a numerical technique which relates the wideband receiver measurements to absolute field strengths using the gains applied by the AGC. This technique is described in detail by *Reeves* [1989]. Gaps in the wideband data are due to the antenna switching pattern.

Very intense wave activity which saturates the wideband receiver is observed within $\sim$ 10 m perpendicular to the beam and in the wake of the beam. The region of receiver saturation is defined as zone 1. Zone 2 contains waves of lower amplitude. In this zone, the amplitude drops off rapidly with distance from the beam. Zone 3 contains beam-produced waves of significantly reduced amplitude compared to zones 1 and 2. The amplitude of the zone 3 emissions decreases gradually with distance. It is the rate of decrease of amplitude with distance which distinguishes zones 2 and 3. Zone 3 emissions are distinguished from background fields by their spectra (Plates 1*a* and 1*b* of *RBN*) and by comparisons of amplitudes for ambient, DC flux tube connection, and Pulsed flux tube connection intervals. It is likely that zone 3 extends out to distances greater than the maximum perpendicular distance from the beam probed by the PDP in these experiments.

Figure 3 shows electric and magnetic field measurements which illustrate the zone structure in the region near the beam ($r_\perp < 30$ m). Broadband wave amplitudes at $\sim$150 Hz are taken from the ELF band of the wideband receiver. Unlike the data from the VLF band shown in *RBN* the ELF band had no frequency switching pattern so both the electric and the magnetic wave amplitudes could be measured near the beam during the DC flux tube connection. The PDP passes closest to the beam at $\sim$0334:10 UT. Modulation of the amplitude due to the spin of the PDP is observed throughout the interval shown here. Zone 1 is easily identified by the large wave amplitudes which are near or above receiver saturation levels. We note that the apparent variation of amplitude within zone 1 may be an artifact of the processing since the amplitude cannot be properly determined from the wideband receiver data when the AGC is saturated. Figure 3 shows that the zone structure and the variation of the broadband wave amplitudes with distance from the beam are similar for the electric and the magnetic

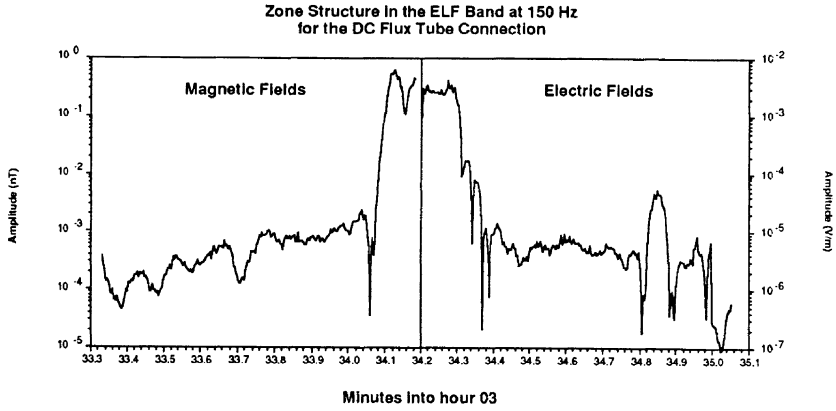

Fig. 3. The amplitudes of broadband magnetic and electric fields at $\sim$150 Hz as measured in the ELF band of the wideband receiver. Magnetic and electric field data are shown on the same plot but with different scales. The PDP passes closest to the beam region at $\sim$0334:10 UT and strong zone 1 emissions are observed around this time. Zone 2 emissions have amplitudes which decrease rapidly with distance from the beam and are observed on the approach to and recession from the beam region. It is seen that the spatial structures are similar for the electric and magnetic fields.

components, providing evidence of the observation of electromagnetic waves produced by the beam.

An overview of the wave fields: Filter bank data. Plate 1 shows the electric field wave data from the PDP filter banks during the DC flux tube connection sequence. (Plate 1 can be found in the special color section in this issue.) Plate 1 is similar to those presented in *GF* and provides a good overview of the wave environment. Spectral intensities (in $V^2/(m^2\ Hz)$) are presented in continuous frequency format by interpolating between values at the filter frequencies. Unlike the VLF wideband receiver, the IMP/Helios and MFR instruments had no automatic gain control (AGC), and the electric field measurements had no antenna switching pattern, so a continuous time record could be obtained. The FPEG is operated continuously from 0330:12 UT to 0337:22 UT. At earlier and later times in the figure, the FPEG is not operated, and the ambient wave fields are observed. At approximately 0334:10 UT the PDP passes closest to the conjunction field line (Figure 1), and the strongest emissions are seen at this time. Periodic modulations of the wave amplitudes due to the rotation of the PDP are observed at all times.

Two distinct sets of beam-produced emissions can be identified. At frequencies between the local lower hybrid frequency and the electron cyclotron frequency ($\sim$ 6.6 kHz and 1 MHz respectively for the DC flux tube connection) a funnel-shaped emission feature is observed. These emissions were identified by *Gurnett et al.* [1986] as quasi-electrostatic whistler mode waves, produced through the Cherenkov resonance, which have wave normal angles near the resonance cone angle. Below $\sim$ 30 kHz, a separate set of broadband wave emissions can be observed. These waves are observed at all locations at which measurements were made. They are referred to as the beam-generated $\mathcal{VLF}$ emissions and are the subject of this investigation. (The designation $\mathcal{VLF}$ is used to differentiate between these waves and other waves, such as the resonance cone waves, which may also be observed at VLF frequencies.)

For the DC flux tube connection, the beam-generated $\mathcal{VLF}$ emissions are comparable in amplitude to the background emissions. However, the beam-generated emissions may be easily distinguished from the background waves in high-resolution spectrograms from the wideband wave receiver because the spectral structure and temporal structure of the ambient and beam-generated waves are quite different (*RBN*). Beam-generated waves may be identified by amplitude alone for the Pulsed flux tube connection sequence because the ambient wave fields were $\sim$ 2 orders of magnitude lower than for the DC flux tube connection. The beam-generated broadband waves had comparable amplitudes for the two sequences. Therefore, in the filter bank data for the Pulsed flux tube connection (Plate 2) both the resonance cone funnel and the broadband $\mathcal{VLF}$ signals are easily distinguished from the background fields. (Plate 2 can be found in the separate color section in this issue.)

Plate 2 shows PDP filter bank data for the Pulsed flux tube connection sequence. It is seen that the broadband wave production and propagation characteristics are similar to the dc beam results. For the Pulsed flux tube connection, the FPEG was turned on at 0411:13 UT when the PDP was near the conjunction field line. The FPEG was turned off at 0418:23 UT. At times when the FPEG was not firing, the ambient fields were observed. Since there were only four filters per decade of frequency, the narrow-band emissions at the pulsing frequency and its harmonics are not well represented in the filter bank data. However, the enhanced amplitude of waves near 1 kHz, as compared to the DC flux tube connection, is attributable to the presence of the narrow-band signals at 1.22 kHz. The narrow-band wave signals are more clearly represented in the wideband receiver data. (See Plate 1 of *RBN*.)

Narrow-band wave observations. Pulsed electron beams injected into space plasmas are observed to generate narrow-band radiation in addition to the broadband emissions which are produced by both pulsed and dc beams. Previous studies have shown that both electric and magnetic narrow-band wave response is observed at the pulsing frequency and harmonics of that frequency. It has also been observed that, although the harmonic structure of the narrow-band radiation may vary, the predictions of Fourier theory are that harmonics for which the harmonic number times the duty cycle of the wave is integral will have zero amplitude. However, spectra from both STS 3 and Spacelab 2 have shown that emissions at these "forbidden frequencies" are frequently observed [*Reeves et al.*, 1988*a*, 1988*b*].

The Pulsed flux tube connection during the free flight of the PDP on Spacelab 2 offered an opportunity to study the production of narrow-band emissions by pulsed electron beams. The format of the pulsing sequence (1.22 kHz, 100-mA, 50% duty cycle, for $\sim$ 7 min while the PDP traversed the conjunction field line) allowed the measurement of wave amplitudes at the harmonic frequencies at various distances from the beam using the wideband wave receiver. The filter bank instruments did not provide sufficient resolution for the study of the narrow-band emissions.

The narrow-band emissions were found to share some common features with the beam-generated broadband waves. Both produce electric and magnetic fields which tend to decrease in amplitude with increasing frequency and with increasing distance from the electron beam. The narrow-band waves were found to have amplitudes which were stronger than the broadband waves by a factor of 5 to 15. The harmonics which lay in the 0–10 kHz band had amplitudes in the range $\sim 10^{-6} - 2 \times 10^{-5}$ V/m and $\sim 10^{-5} - 5 \times 10^{-4}$ nT for the odd harmonics. The even, "forbidden," harmonics were most clearly observed with the magnetic antenna and were generally an order of magnitude lower in amplitude. It was also found that the ratio of the amplitude of the narrow-band emissions at the fundamental frequency (1.22 kHz) to the amplitude of the broadband emissions at frequencies near the fundamental (1.7-1.8 kHz) was a fairly constant function of the distance from the electron beam (*RBN*).

3. Analysis of Electron Beam-Plasma-Wave Interactions

The observations of background and beam-generated waves during the free flight of the plasma diagnostics package contain a rich and complex range of phenomena. In the following sections we present an analysis and interpretation of several classes of phenomena. Observations of narrow-band waves, produced by pulsed beams, are compared with the predictions of theory. Analysis of the amplitudes measured during the PDP free flight at different frequencies and distances from the beam allow identification of the wave mode and resonance condition. The electromagnetic component of the broadband waves which are observed for both

pulsed and dc beam operation is interpreted within the context of a single-ion, cold plasma treatment. The effects of a second ion species are considered, and possible contributions to the broadband wave observations from electrostatic waves are discussed. Finally, the ratios of electric and magnetic wave amplitudes are investigated, and an estimate of the radiated power in the narrow-band waves is presented.

The primary observations upon which we base this investigation are as follows: (1) Intense broadband ELF and VLF waves are produced by 1-keV pulsed and dc electron beams. (2) The broadband $\mathcal{VLF}$ emissions contain electric and magnetic components. (3) The broadband $\mathcal{VLF}$ waves have an upper cutoff frequency. (4) The electric and magnetic wave amplitudes are a function of both frequency and distance to the beam. (5) The observed wave amplitudes define three spatial zones. (6) Pulsed electron beams produce narrow-band emissions at the harmonics of the pulsing frequency which are superimposed upon the broadband spectrum.

Narrow-Band Emissions

A theory of narrow-band, near-field radiation from pulsed electron beams was developed by *Harker and Banks* [1987]. (This paper will be referred to as "*HB*.") It contains expressions for the electric field amplitudes produced by square-wave-modulated electron beams with known energies, currents, and pitch angles measured at any distance larger than one gyroradius from the beam. These expressions can be applied to experimental conditions by using the parameters which are appropriate for the conditions at the time of the experiment. *Neubert and Harker* [1988] have extended this theory to predict the narrow-band magnetic field amplitudes. Because the theory treats only coherent production of radiation, no broadband wave amplitudes are predicted.

The exact results for the amplitude of narrow-band radiation from a pulsed electron beam are complicated, but we can summarize some of the general features. Since the theory predicts the near-field wave amplitudes, we are justified in applying it to our observations without reservations about neglecting the near-field contributions. The mathematical treatment assumes a perfectly coherent infinitely long, thin beam in the half-space $z > 0$. The value of the parallel index of refraction is found from the resonance conditions $k_{\|} = (\omega - s\omega_{ce})/v_{\|}$. Here, $\|$ refers to $\mathbf{B_0}$ (the ambient magnetic field), k is the wave number, v is the beam velocity, $s = 0$ is the Cherenkov or Langmuir resonance, $s = 1$ is cyclotron resonance, and $s = -1$ is anomalous cyclotron resonance. The electric field amplitudes are related to the electron beam current density through a radiation condition which can be expressed in frequency wave number space as a function of $k_{\perp}$, the perpendicular wave number. A contour integration over $k_{\perp}$ selects the self-consistent wave normal angles, and the fields are transformed back into coordinate space. Results are derived for both (complex) values of $k_{\perp}$ (labeled roots 1 and 2 in *HB*) for each of three resonance conditions. For the whistler mode, root 1 is the resonance cone solution, and the wave normal angle $\theta \approx \theta_{res}$. Root 2 is the central hump solution, and $\theta < \theta_G$, where θ_G (the Gendrin angle) is the wave normal angle for which the parallel index of refraction is minimum. The three components of the electric field can then be evaluated numerically for a variety of experimental conditions as is done below.

The theory of *HB* makes no a priori restrictions on which wave modes will be produced. Rather, the predictions are that all wave modes are produced and should appear superimposed upon one another. In order to determine which wave mode and which resonance condition is responsible for the production of the observed narrow-band signals, the measurements of the wave amplitudes for the various harmonics at various distances are compared with the predicted amplitudes for the conditions appropriate for the experiment. For the conditions of the Pulsed flux tube connection, $f_{pe} \approx 1.6$ MHz, $f_{ce} \approx 0.63$ MHz, $f_{LHR} \approx 3.6$ kHz, and the pulsing frequency $f_0 = 1.22$ kHz. At 1.22 kHz, only the $s = 0$, root 2 predictions have real solutions. The fields for $s = \pm 1$ (cyclotron and anomalous cyclotron) are evanescent because the resonance condition cannot be satisfied. For example, under experimental conditions and $s = -1$, the resonance occurs at $n_{\|} \approx 8000$, but the value of the parallel index of refraction is $n_{\|} \approx 56$. The $s = \pm 1$ resonances may be satisfied only at frequencies above the lower hybrid frequency. Likewise the $s = 0$ root 1 solutions are evanescent for $f < f_{LHR}$.

Above the lower hybrid the root 1 solutions of the s = ± 1 resonances become highly oscillatory functions of frequency for frequencies below 30 kHz, and no exact predictions can be made. The oscillations in wave amplitude for the $s = \pm 1$, root 1 solutions have maxima which are greater than 1 V/m and zeros which are separated by only a few hertz. Waves in these modes must be treated using hot plasma theory. Although it is possible that the observed narrow-band beam emissions are due to $s = \pm 1$ resonance but are observed with amplitudes well below those predicted by theory, it is unlikely because the wavelengths are much smaller than the dimensions of the probes. We will see below that much better agreement between measurement and theory is found for the $s = 0$, or Cherenkov, mode.

The total electric field strengths predicted by *HB* for the $s = 0, 1, -1$, root 2 and the $s = 0$, root 1 solutions are presented in Figure 4. The figure shows the predicted ampli-

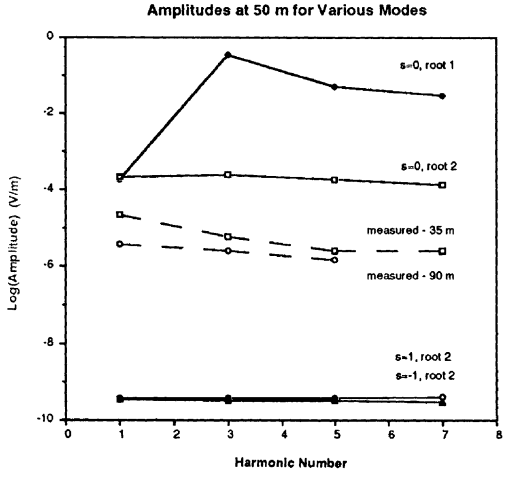

Fig. 4. The amplitude of narrow-band harmonics of the 1.22-kHz pulsing frequency. The log of the electric field wave amplitude is plotted versus harmonic number for the predictions using the theory of *HB* for the $s = 0$, roots 1 and 2, and for the $s = \pm 1$, root 2 solutions. Predicted amplitudes were calculated for a perpendicular distance of 50 m from the conjunction field line. Measured amplitudes (dashed lines) are plotted versus harmonic number for the observations at perpendicular distances of 35 and 90 m.

tude as a function of harmonic number for a perpendicular distance of 50 m from the beam (solid lines). The observed wave fields measured at 35 m and 90 m from the beam are plotted with dashed lines. The predicted amplitude of these four wave modes (solid lines) and the measured amplitude for the fundamental (dashed line) are plotted as a function of distance from the conjunction field line in Figure 5. These two figures allow comparison of the variation with frequency and the variation with perpendicular distance for predictions and measurements for the different wave modes. Root 1 represents resonance cone propagation, and solutions are imaginary below the lower hybrid resonance and real above it. Root 2 has real solutions throughout the frequency range of interest and describes waves which lie in the central hump of the index of refraction surface. The $s = \pm 1$, root 2 solutions are found to have amplitudes well below observed values.

Figures 4 and 5 show that reasonable agreement between observations and the predictions of *HB* are found for the $s = 0$, root 2 solutions. The variation of amplitude with harmonic number and with perpendicular distance to the beam more accurately follows the observed variation for that mode than for any of the other three modes. This comparison suggests that the observed narrow-band waves are whistler mode radiation produced through the Cherenkov resonance and that central hump rather than resonance cone solutions are dominant.

Figure 6 shows a comparison of the measured wave amplitudes as a function of harmonic number for the electric and magnetic fields at various distances from the beam with the predictions for the $s = 0$, root 2 solutions. The predicted amplitudes are shown by light shaded bars while the measured amplitudes are dark. The amplitudes of the harmonics of 1.22 kHz which lie in the 0–10 kHz band are plotted.

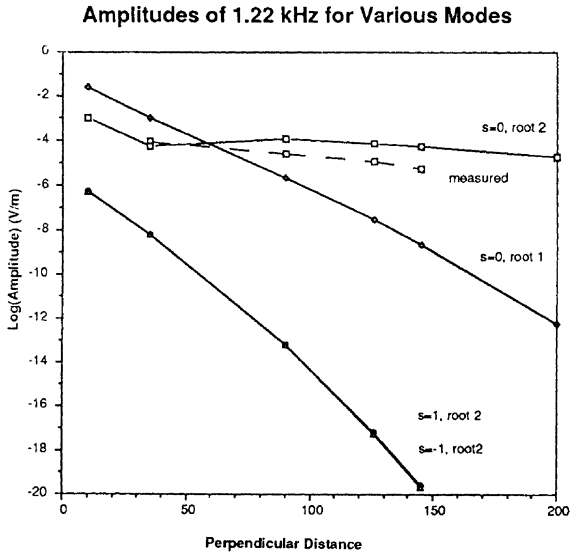

Fig. 5. The variation of amplitude with perpendicular distance to the conjunction field line for the 1.22-kHz fundamental frequency. The log of the electric field wave amplitude is plotted versus harmonic number for the predictions using the theory of *HB* for the $s = 0$, roots 1 and 2, and for the $s = \pm 1$, root 2 solutions. The $s = 0$, root 1 and the $s = \pm 1$, root 2 solutions represent

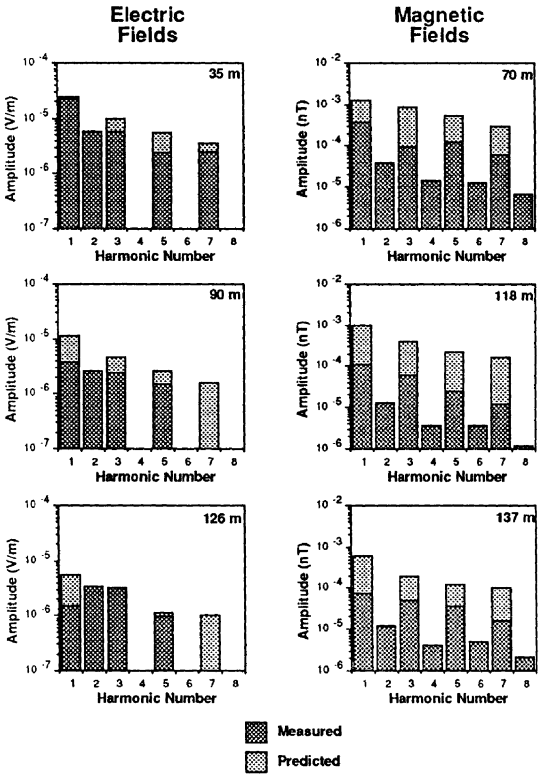

Fig. 6. The predicted (light bars) and measured (dark bars) narrow-band wave amplitudes during the Pulsed flux tube connection sequence. The electric and the magnetic fields at harmonics of the 1.22-kHz pulsing frequency, measured at various distances from the beam region, are shown. No amplitudes are predicted for the even harmonics of the 50% duty cycle pulsings, but some response is measured. Predicted amplitudes for the odd harmonics are generally higher than measured by a factor of ~30.

Since the FPEG was pulsed with a 50% duty cycle, the even harmonics are "forbidden," and there are no predicted amplitudes for those harmonics. Where no measured values are given, the narrow-band signals were indistinguishable from the broadband signals.

At all distances at which the narrow-band fields were measured, the theory and measurement show the best agreement for the Cherenkov, root 2 solutions. For those solutions, *HB* predict electric and magnetic field amplitudes which are greater, but less than 30 times greater, than the measured field amplitudes at all distances and for all harmonics. The general features observed in the measured data are reproduced in the calculations. The electric field amplitudes range from 10^{-6} to 10^{-4} V/m, and the magnetic field amplitudes range from 10^{-4} to 2×10^{-3} nT for harmonics in the 0–10 kHz band. For both the electric and the magnetic antennas, the amplitude of the narrow-band harmonics decreases with increasing distance from the conjunction field line and, at all distances, the amplitude decreases for increasing harmonic numbers.

The difference in measured and predicted amplitudes could be accounted for by a reduction in coherent beam current from the nominal 100-mA level. This reduction could

occur through such mechanisms as scattering or diffusion of beam electrons, beam current cancelation by return currents, or the production of a virtual cathode as suggested by numerical simulations done by *Winglee and Pritchett* [1987, 1988]. Data processing may also contribute to the difference. Measured amplitudes are time averaged while predicted amplitudes are the magnitude of the wave vector. On a scale which ranges over many orders of magnitude, agreement better than a factor of 30 is considered quite good.

It is also worth noting the qualitative differences between the measured and predicted wave fields. In Figure 6 the most notable difference is the presence of measured emissions at the even, forbidden, harmonics which are not predicted by theory. This suggests a loss of the idealized square-wave coherence assumed by the theory. We also note the enhanced amplitude of the second and third harmonic for the electric fields measured at large distances from the beam. This enhancement is observed only with the electric antenna and suggests the presence of electrostatic contributions from the wave field. Since these harmonics surround the local lower hybrid frequency (3.6 kHz for this sequence), it is possible that these contributions are from lower hybrid waves.

The results of *HB* are used here with the following caveat. It has been determined that the contour integration over $k_\perp$ in *HB* contains branch cuts in addition to simple poles. *HB* evaluates only the contributions to the integral from the simple poles, which correspond to surface waves, and therefore the solution is incomplete. In addition to the field components calculated, there will be field contributions due to terms which arise from the inclusion of these branch cuts which correspond to ray propagation. Those contributions can be evaluated and will be presented in an upcoming paper. It has been determined that the contributions from the branch cuts will become increasingly significant as the distance from the beam increases, but the effect at smaller distances has not been determined. For example, we note that in Figure 4 the predicted amplitudes of the $s = 0$, root 1 solutions are much stronger than what was observed for harmonics which lie above the lower hybrid frequency (e.g., the third harmonic and higher). This may indicate that observations were made in a region for which the theory of *HB* does not strictly apply for waves in that mode. We note that the resonance cone waves at these frequencies have relatively short wavelengths compared to the distance of the PDP from the beam and therefore the contributions from the branch cuts are likely to be significant. In this paper we conclude only that the theory of *HB*, as it stands, provides good agreement with experimental observations for the $s = 0$, root 2 mode which describes Cherenkov resonance with wave normal angles less than the Gendrin angle.

Broadband Waves

Identification of the wave modes. The theory of *HB* treats only narrow-band emissions from perfectly coherent beams. In order to investigate the production of broadband waves, a similar but more qualitative theory is required. We begin such an analysis by considering the predictions of a single-ion, cold plasma theory. At the space shuttle orbital altitude of 325 km the dominant ion species is O^+. Thus, we will consider a two-component (O^+ and e^-) cold plasma in the frequency range $f < f_{ce}$ where f_{ce}, the electron cyclotron frequency, $\approx$ 1 MHz. The observation of strong beam-generated magnetic broadband waves suggests that electromagnetic waves were measured. The wave fields also contain contributions which appear to be electrostatic (such as lower hybrid or ion acoustic waves), and quasi-electrostatic (such as the whistler mode resonance cone waves), but initially we will discuss only the electromagnetic contributions.

Schematic of the Index of Refraction Branches

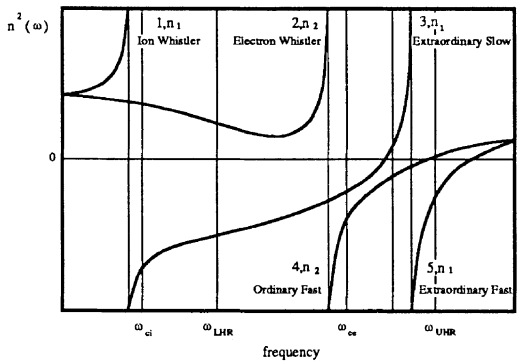

Fig. 7. A schematic diagram of the square of the index of refraction as a function of frequency for arbitrary wave normal angles with the various wave branches labeled. The case $\omega_{pe} > \omega_{ce}$ is indicated.

Following the treatment of *Al'pert* [1983] we consider the cold plasma dispersion curves $n^2(\omega)$, where n is the complex index of refraction (Figure 7). We also consider plane wave solutions to the wave equation. Since the dispersion relation is quadratic in n^2, there are two roots at any given frequency, n_1 and n_2, as given by the sign before the discriminant. In the frequency range $\omega_{ci} < \omega < \omega_{ce}$, where ω_{ci} is the ion cyclotron frequency, only the n_2 root is real, and this branch is the whistler mode. Most of the Spacelab 2 wave data fall in this range. The index of refraction, n, is a function of the angle, θ, between the wave normal direction and the direction of the magnetic field. For $\omega < \omega_{LHR}$ (the lower hybrid frequency), the index of refraction surface, $n_2(\theta)$, is closed, and n_2 is finite for all θ. For higher frequencies the surface is open, and $n_2(\theta)$ becomes infinite at the resonance cone angle, θ_{res}.

For both narrow-band and broadband emissions the resonance condition for the interaction of beam electrons with plasma waves is $k_\parallel = (\omega - s\omega_{ce})/v_\parallel$. Therefore it is again the case that for $\omega < \omega_{LHR}$ only the $s = 0$ (Cherenkov) resonance condition can be satisfied and only the root 2 (central hump) solutions are real. For frequencies above the lower hybrid resonance frequency the cyclotron and anomalous cyclotron resonance conditions can be satisfied because the index of refraction becomes infinite on the resonance cone. Unlike the narrow-band emissions which occur only at discrete frequencies the broadband emissions span a range of frequencies so the behavior across the lower hybrid can be used to help identify the wave mode. In the VLF spectra from Spacelab 2 we find that, in general, there is no distinct change in wave amplitude or spectral shape at the lower hybrid frequency (*RBN*). *Gurnett et al.* [1986] have already identified the funnel shaped emission observed during the DC flux tube connection as Cherenkov radiation. Those waves correspond to the resonance cone solutions (root 1).

However, the resonance cone solutions cut off at the lower hybrid while the central hump (root 2) solutions are continuous across f_{LHR}; thus the most likely source of the electromagnetic component of the $\mathcal{VLF}$ emissions is also the Cherenkov resonance but with wave normal angles in the central hump.

Basic predictions. To explore this idea in the context of Spacelab 2 observations we consider the characteristic features expected from the Cherenkov, central hump waves. Specifically we consider the conditions which existed during the DC flux tube connection sequence. (The instrumental and plasma parameters for various electron beam wave generation sequences on Spacelab 2 are given in Table 1 of *RBN*.) Using $v_{\|} = 1.9 \times 10^7$ m/s for a 1-keV beam directed along the field line, the Cherenkov resonance condition, $s = 0$, gives $n_{\|} = 16$, independent of the frequency of the waves. Using the value $n_{\|} = 16$ one can calculate the wave normal angle (or phase velocity angle), θ, and the ray angle (or group velocity angle), α. The ray angle then determines the propagation characteristics of the waves.

The ambient magnetic field strength and background electron density during the DC flux tube connection were $B_0 = 0.40$ gauss (G) and $n_e = 10^5$ cm^{-3}, respectively. Using these values for the $s = 0$ resonance and $\theta < \theta_G$ we can calculate the expected ray angles at various frequencies. At low frequencies ($f = 100$ Hz for example) the condition $n_{\|} = 16$ picks out very large wave normal angles, $\theta \approx 90°$, which on a closed index of refraction surface implies large ray angles, $\alpha \approx 90°$. This situation is represented schematically in Figure 8*a*. For $f = 1$ kHz, the index of refraction surface is flatter, $\theta < 90°$, and α becomes small, $\alpha \approx 5°$ (Figure 8*b*). At higher frequencies a resonance cone develops and there are two solutions which satisfy $n_{\|} = 16$: resonance cone ($\theta \approx \theta_{res}$) and central hump ($\theta < \theta_G$). The central hump solutions have moderate ray angles. At 15 kHz, $\theta \approx 60°$ and $\alpha \approx 20°$ (Figure 8*c*). As we continue to increase the frequency, the index of refraction surface gets lower at small angles, and the central hump wave normal angle picked out by the Cherenkov resonance condition approaches zero. At ~ 30 kHz, $\theta \approx 0°$ and $\alpha \approx 0°$ (Figure 8*d*). For even higher frequencies, the value of the parallel index of refraction for $\theta < \theta_G$ becomes less than 16, and only resonance cone propagation will satisfy the $s = 0$ resonance condition (Figure 8*e*).

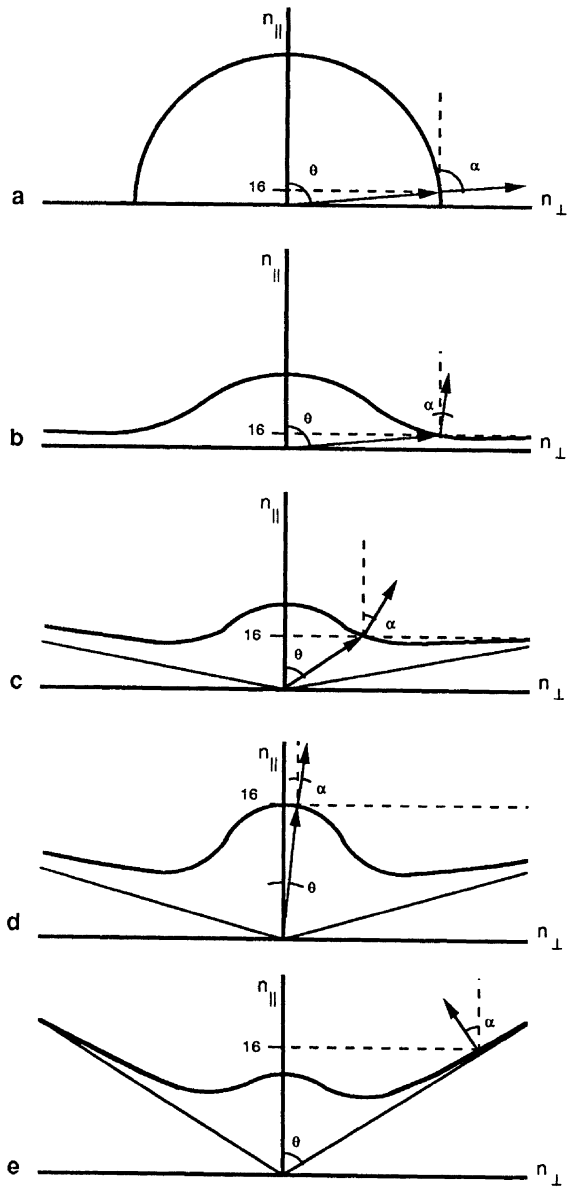

Fig. 8. A schematic of the index of refraction surfaces for various frequencies showing the wave normal and ray angles picked out by the Cherenkov resonance condition. (*a*) For low frequencies, $n_2(\theta)$ is a closed surface, and for $n_{\|} = 16$, $\theta \approx 90°$, and $\alpha \approx 90°$. (*b*) For frequencies $f \geq f_{LHR}$, $n_2(\theta)$ is an open surface. For $\theta < \theta_G$, $n_{\|} = 16$ picks out wave normals in the central hump. For $f \sim f_{LHR}$, θ is large, and $\alpha \approx 0°$. (*c*) As f increases, θ decreases, and α increases up to a maximum of $\sim 20°$. (*d*) For $f \rightarrow 30$ kHz, $\theta \rightarrow 0°$, and $\alpha \rightarrow 0°$. (*e*) Above a critical frequency the resonance condition $n_{\|} = 16$ can no longer be satisfied for wave normal angles $\theta < \theta_G$, and only resonance cone propagation is possible.

To help visualize the relationship between frequency and distance to the beam, the predicted propagation region for waves generated through the Cherenkov resonance is shown schematically in Figure 9. The propagation region for $\mathcal{VLF}$ radiation is determined as described above. Frequency has been plotted versus distance rather than time, and angles have been converted into distance by multiplying the sine of the ray angle by 200 m, which is a nominal value for the distance from the orbiter to the PDP. The ray angle, and hence the propagation region, are a function of frequency.

Figure 9*a* shows the region of propagation predicted for Cherenkov, whistler mode waves. The limits of propagation of the resonance cone emissions which produce the funnel-shaped feature between f_{LHR} and f_{ce} are plotted with a solid line. The limit of the predicted region of propagation of the electromagnetic component of the $\mathcal{VLF}$ waves is plotted with a bold line. These lines define a region in frequency and distance (or equivalently time) in which propagating radiation is expected. Thus, according to the simple model discussed above, a receiver which follows a trajectory perpendicular to the conjunction field line should detect $\mathcal{VLF}$ radiation at all distances within the propagation region. Outside the propagation region, only ambient fields are predicted by this simple model. Within the propagation region the amplitude would be expected to decrease steadily with distance.

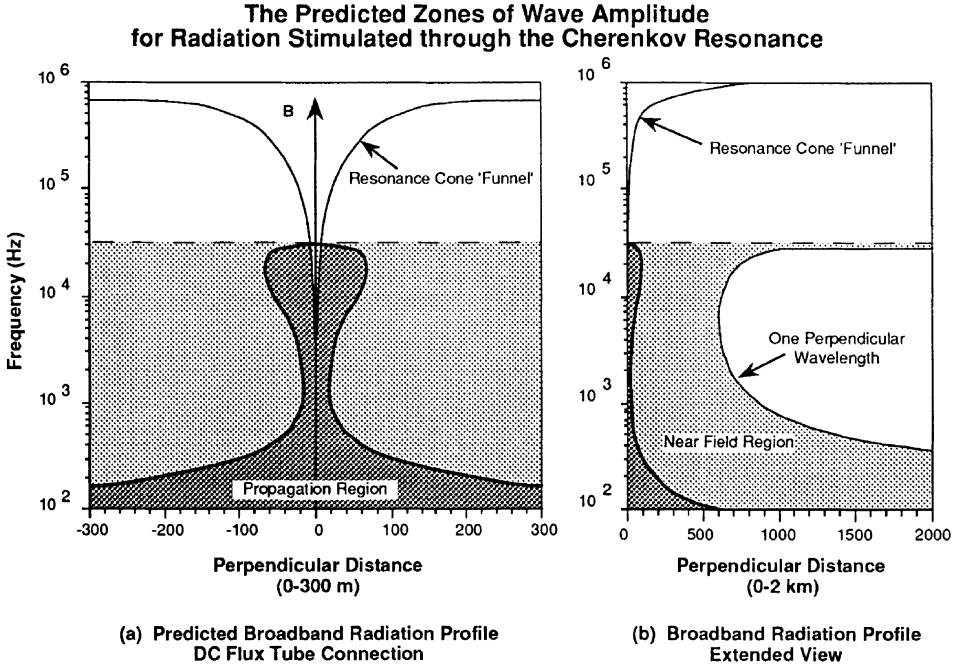

Fig. 9. A schematic representation of the propagation of whistler mode waves generated through the Cherenkov resonance as predicted from cold plasma theory. Zone 1 is identified as being associated with a region of the plasma which is highly disturbed by the injection of the electron beam. Because of its small extent, zone 1 is not indicated in this figure. The limit of zone 2, which contains propagating waves with wave normal angles less than the Gendrin angle, is indicated with a bold line and is labeled "propagation region." The limits of the resonance cone and zone 2, $\mathcal{VLF}$, propagation regions are indicated by plotting the sine of the ray angle times 200 m. The dashed line indicates the predicted limits of zone 3 represented by a distance equal to one perpendicular wavelength from the conjunction field line. Although this figure implies distinct borders, observations show that the transitions from one zone to another are smooth.

Figure 9*b* shows an important modification to the simple model, namely near-field effects. Figure 9*b* shows the same curves as Figure 9*a* but on a larger scale. Also shown is the perpendicular wavelength ($\lambda_\perp$) as a function of frequency for the $\mathcal{VLF}$ emissions. (For the resonance cone emissions, $\lambda_\perp$ is small compared to the distance and is not plotted.) This figure shows that all the PDP data were taken within the near field of these waves.

It is apparent from Figure 9*a* that the observed wave amplitudes are not completely explained by the predictions of the basic model. If measurements were made in the far field of the beam, then the observed wave contributions at various frequencies would be expected to have an abrupt cutoff at the limits of the propagation region. However, as Figure 9*b* indicates, the measurements were not made in the far field for these $\mathcal{VLF}$ emissions. What we would expect in this case is a superposition of wave fields. A radiation field should exist within the propagation region. Nonpropagating waves should also be observed throughout the near-field region which includes the propagation region and extends beyond the maximum distance probed.

Figure 9 also suggests that we consider the different zones of wave amplitudes observed in the Spacelab 2 data in terms of the propagation characteristics. We cannot predict the amplitudes of broadband radiation from electron beams as we did for the narrow-band emissions. However, we can readily identify the zone 3 emissions as near-field contributions. The stronger electric and magnetic fields observed near the beam cannot be conclusively identified. Although those waves appear to be electromagnetic and are confined to a limited spatial extent, the filter bank data do not show a clearly defined propagation region. Lacking measurements made in the far-field region, the production of propagating broadband radiation can only be inferred from the observation of near-field waves which appear to be produced by the resonant Cherenkov interaction of the beam with the plasma.

Comparing the predictions of a single-ion cold plasma treatment of the broadband radiation with the observations from the Spacelab 2 free flight shows good agreement. Whistler mode waves have two branches. The resonance cone waves produce the funnel between f_{LHR} and f_{ce}. The central hump waves may be associated with the $\mathcal{VLF}$ emissions. The $\mathcal{VLF}$ waves are continuous across the lower hybrid resonance and have an upper cutoff at $\approx$ 30 kHz. Both characteristics are consistent with a Cherenkov resonance for a 1-keV electron beam. The presence of zones of wave amplitude may also be understood in terms of the presence of both propagating and near-field waves.

The effects of two ion species. Comparison of the observations of broadband electron beam-generated waves with the predictions of a two-component cold plasma theory has

yielded agreement on some of the basic features observed in the data. The experimental situation is, however, considerably more complicated than the model used for the predictions. For example, the model neglects ion species other than O^+ (notably H^+), the finite temperature of the plasma, disturbance of the ambient plasma by thruster emissions, vehicle outgassing, and the 7.7-km/s velocity of the orbiter and the PDP through the medium. We consider here some of the observed wave features which are not predicted by the model. In particular we note the effects of the modulation of the wave signals by the spin of the PDP, the effects of the presence of H^+, and the contributions of electrostatic waves.

Although the amplitude of broadband waves is observed to decrease with distance from the beam, there is considerable variation in amplitude superimposed on the steady decline. (Note, for example, the low-frequency waves in Plates 1 and 2 and in Figure 3.) Most of this variation can be attributed to the effects of spin modulation of the PDP. The electric and magnetic antennas were both single axis and measured fields in the spin plane of the PDP which rotated with a period of ~13 s. Some work has been done to extract the polarization of the waves from the spin modulation of the signals and the relative orientations of the orbiter, the geomagnetic field, and the PDP antennas [*Neubert et al.*, 1989*b*]. However, accurate determination of the polarization is quite difficult and does not substitute for vector field measurements.

We also note that, in addition to O^+, there is an appreciable amount of H^+ at orbiter altitudes. With H^+ present, there is an additional ion cyclotron resonance which lies at 611 Hz for $B_o = 0.40$ G. The ray angles predicted from cold plasma theory (Figures 8 and 9) show the same general characteristics as for the single-ion species case for frequencies above the H^+ ion cyclotron frequency, $f_{ci}(H^+)$. For frequencies just below $f_{ci}(H^+)$, the model ray angle drops to zero but then rapidly increases to large angles with decreasing frequency until the O^+ ion cyclotron frequency at 38 Hz.

Calculations using the international reference ionosphere (IRI) model [*Bilitza*, 1986] for the conditions during the DC flux tube connection give $N_{H+} = 1\% N_{e-}$ and $N_{O+} = 99\% N_{e-}$. In the ELF band (~0–1 kHz) some effects of the presence of a second ion species may be observed. These observations include detection of a two-ion cutoff in the ELF band [*Reeves*, 1989]. For the purposes of this study we note that the H^+ concentration is not large enough for it to have significant impact on the index of refraction surfaces at VLF frequencies. At 500 Hz a two-ion calculation of the index of refraction at wave normal angles of 30° with $N_{H+} = 10\% N_{e-}$ is 36% different from the calculation using only O^+ and e^-. At 1 kHz the difference has dropped to 7%, and at 5 kHz it is 0.7%. The general features which are discussed in the observed data are predicted from both single-ion and two-ion calculations.

Electrostatic Contributions. We have also considered the possible contribution to the observed electric field from electrostatic waves such as ion acoustic waves. Purely electrostatic contributions do not account for the enhancement of the wave magnetic field above ambient levels or the wave features observed in the IMP/Helios and wideband receiver data and therefore would constitute an additional set of wave fields which could be detected along with the whistler mode, resonance cone, and central hump wave fields. Electrostatic waves could be produced either by the primary beam electrons or by lower-energy beam or ambient plasma electrons. *Farrell et al.* [1988] have proposed that electrostatic oscillations at the plasma frequency are responsible for bunching of the beam electrons, which in turn provides a mechanism for coherent Cherenkov resonance. They cite the presence of electric fields at $f \approx f_{pe}$ or f_{UHR} as consistent with this conclusion (see Plates 1 and 2). Simulations done by *Winglee and Pritchett* [1987] also suggest the presence of space charge oscillations at $f \approx f_{pe}/\sqrt{3}$ which occur within a short distance between the source and a beam stagnation front. *Okuda and Ashour-Abdalla* [1988] have also predicted low frequency ion acoustic waves using a numerical simulation. They point out that the high-energy ($v << v_{thermal}$) beam electrons cannot directly couple to low-frequency ion acoustic waves but that low-energy electrons can. Therefore it is likely that there is little electrostatic contribution to the observed $\mathcal{VLF}$ waves from the primary beam electrons.

There are, however, several possible sources of low-frequency waves from low-energy electrons. One of the most important is the return current electrons which are necessary to maintain charge balance on the orbiter. *Hawkins* [1988] determined that for Spacelab 2 the majority of return current was collected on the orbiter engine bells. No waves from such a source could be identified in the wave data. *Frank et al.* [1989] have shown that an additional population of low-energy electrons exist in the wake of the primary electron beam. The beam wake was measured with the PDP LEPEDEA particle detectors and was found to be a sheet aligned with the geomagnetic field which was ≈ 20 m wide and which extended more than 170 m in the antivelocity direction. Velocity distributions showed that the low-energy electrons in the beam wake were generally directed in the opposite direction from the primary beam. *Frank et al.* [1989] also show that strong electric fields are observed in the beam wake and conclude that these are probably electrostatic ion acoustic waves.

Figure 10 represents a view of the beam wake looking along the magnetic field direction. The coordinate system is $\mathbf{V}_\perp$ (where $\mathbf{V}_\perp$ is the component of the shuttle velocity perpendicular to the geomagnetic field $\mathbf{B}_0$) and $\mathbf{V}_\perp \times \mathbf{B}_0$. The beam is represented by a circle of radius 5 m which is the maximum gyroradius for a 1-keV beam during the flux tube connection sequences. Based on the results of *Frank et al.* [1989] the beam wake is shown as a 20-m-wide region extending in the $-\mathbf{V}_\perp$ direction. The trajectory of the PDP in this coordinate system is plotted for the two flux tube connections. One point is plotted each minute starting at 0410 UT for the pulsed case and 0332 UT for the dc case. The trajectories are plotted with bold lines during the intervals in which intense VLF electric fields were observed. These times are estimated from Plates 1 and 2 using 10^{-7} V^2/(m^2 Hz) as an arbitrary level of signal strength. (This level corresponds to the red regions of Plates 1 and 2.)

Figure 10 provides evidence that the enhanced electric fields are produced by electrons in the beam wake. The region in which electric fields of greater than 10^{-7} V^2/(m^2 Hz) were observed corresponds well with the measured extent of the beam wake for both flux tube connection sequences. We note that for the pulsed case the FPEG was not operated as the PDP entered the beam wake so the bold line begins at FPEG turn-on. Electrostatic waves in the beam wake may be responsible for the asymmetries in electric signal strength with respect to the conjunction field line and the relatively

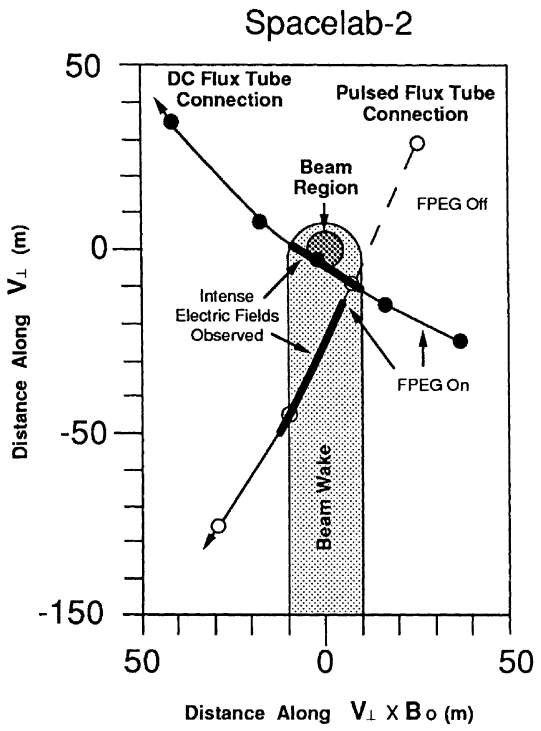

Fig. 10. The correlation of strong electric fields and beam wake structures is shown in a coordinate system defined by the magnetic field B_0 and the perpendicular component of the orbiter velocity vector, $V_\perp$. One point is plotted every minute starting at 0410 UT for the Pulsed flux tube connection and 0332 UT for the DC flux tube connection. Trajectories are plotted bold where the strongest electric fields are measured. The extent of the beam wake region is based on the results of *Frank et al.* [1989].

long duration and spatial extent of the intense fields for the Pulsed flux tube connection compared to the DC flux tube connection. Finally we note that obliquely propagating ion acoustic waves have been observed to be produced in laboratory experiments by drifting electrons in a warm magnetoplasma [*Gekelman and Stenzel*, 1978]. Therefore it is also possible that electrostatic waves produced in the beam wake could also contribute to the fields observed outside that region.

The Ratio of the Electric and Magnetic Field Amplitudes

Observations of magnetic fields produced by the injection of electron beams into space plasmas suggest the production of an electromagnetic component to the beam-generated wave fields. Analysis of the three zones of wave amplitudes shows that similar spatial structures are observed in the electric and magnetic field amplitudes and that some of the observed wave features are consistent with the predictions of cold plasma theory for electromagnetic waves. Observations of strong electric fields which are correlated with the beam wake region indicate the production of electrostatic waves which may be ion acoustic. In this section we consider the ratio of the observed electric and magnetic field amplitudes in order to assess the relative contributions of the two types of waves.

From Maxwell's equations, the wave electric and magnetic field vectors are related through $\mathbf{n} \times \mathbf{E} = c\mathbf{B}$. For a 1-kHz wave with $n_\parallel = 16$ and $B_0 = 0.40$ G, $n_e = 10^5$ cm^{-3} we find that $|\mathbf{n}| = n = |cB/E_\perp| = 316$ where $E_\perp$ is perpendicular to $\mathbf{n}$. On Spacelab 2, vector wave field measurements were not possible. Therefore we need to calculate the ratio $c\langle B\rangle/\langle E\rangle$ where $\langle B\rangle$ and $\langle E\rangle$ are the time averaged amplitudes of the magnetic and electric fields. Knowing the wave normal angle of radiation at a particular frequency, one can use Maxwell's equations to solve for the vector components of the electric and magnetic wave fields. Choosing a coordinate system in which the geomagnetic field defines the z axis and $\mathbf{k}$ lies in the x-z plane, and using conditions for the DC flux tube connection sequence and frequencies near 1.22 kHz we find that the wave normal angle is nearly 90°. The wave electric field has its largest component along the x axis and virtually no component along the geomagnetic field. The wave magnetic field has its largest component along the direction of the geomagnetic field but also has a component along the y axis. Since the PDP rotates with its antennas in a plane containing the geomagnetic field, it is appropriate to consider the time average over all three components of the wave fields. Doing this we find that the average, $c\langle B\rangle/\langle E\rangle$, is less than $cB/E_\perp$ by a factor of ~ 10.

Then for n of order 100, we would then expect ratios of $c\langle B\rangle/\langle E\rangle$ of order 10 for the electromagnetic component of the observed fields. Narrow-band emissions during the Pulsed flux tube connection sequence were determined to have a ratio $c\langle B\rangle/\langle E\rangle$ of order 10 (*RBN*). Comparison of the average magnetic and electric field amplitudes of natural whistlers observed during ambient conditions also gives values of $c\langle B\rangle/\langle E\rangle$ which are of order 10. Therefore we conclude that the narrow-band emissions are electromagnetic waves without significant contributions from electrostatic fields.

For the broadband emissions the situation is more complicated. At most distances for which $c\langle B\rangle/\langle E\rangle$ can be calculated, it is only of order 1. However, for the DC flux tube connection, $c\langle B\rangle/\langle E\rangle$ for broadband emissions could be determined at closer distances (zone 2) using the ELF band data. These measurements give $c\langle B\rangle/\langle E\rangle$ of order 10.

For wave fields consisting of only whistler mode Cherenkov radiation one would expect $c\langle B\rangle/\langle E\rangle$ to be the same for broadband and narrow-band emissions at all distances. Purely electrostatic fields could not account for the observed magnetic field structure. Therefore it appears that the measured broadband wave fields include both contributions. Within zone 2 the measured value of $c\langle B\rangle/\langle E\rangle$ suggests that the electromagnetic fields are dominant. Outside zone 2 but within the beam wake it appears that electrostatic waves produce the most intense electric fields. In zone 3 the measurements of $c\langle B\rangle/\langle E\rangle$ may indicate that electromagnetic and electrostatic waves are both observed. More extensive investigation could be accomplished by simultaneous three-axis measurements of the wave field. The wideband receiver measurements from Spacelab 2 were neither simultaneous nor three-axis. The IMP/Helios instrument provided periods of simultaneous electric and magnetic field measurements, but without detailed knowledge of the orientation of the receivers at a particular time the electromagnetic char-

acter of the observed radiation cannot be investigated more rigorously than has been done here.

Radiated Power

The lack of simultaneous three-axis field measurements also complicates rigorous determination of the Poynting flux, $\mathbf{S} = \frac{1}{\mu_0}\mathbf{E} \times \mathbf{B}$. However, $\mathbf{B}$ has its maximum along the magnetic field line (B_0), and $\mathbf{E}$ has its maximum components perpendicular to B_0. Thus if E_{max} and B_{max} are the maximum amplitudes measured during the spin period of the PDP, then $\frac{1}{\mu_0}E_{max} \cdot B_{max}$ gives an estimate of $|\mathbf{S}|$. For the narrow-band emissions at the 1.22-kHz fundamental frequency during two antenna periods from the Pulsed flux tube connection, $\frac{1}{\mu_0}E_{max} \cdot B_{max}$ is of order 10^{-12} W/(m^2 Hz) for a 12-Hz-wide amplitude component. E_{max} is measured at 0411:48 UT, and B_{max} is measured at 0412:36 UT. At those times the PDP was 22 m and 61 m from the conjunction field line respectively. The quantity $\frac{1}{\mu_0}E_{max} \cdot B_{max}$ is a very rough estimate of $|\mathbf{S}|$, but it is comparable with the predictions of *Bell* [1968] who predicted powers up to 10^{-10} W/(m^2 Hz) for coherent emissions with a coherence length of 10 m and 10^{-18} W/(m^2 Hz) for incoherent emissions. One can also compare this value with the calculations of *Farrell et al.* [1988]. They give a value for the total power radiated by the beam in the form of broadband, whistler mode, resonance cone radiation over a 200-m length of the beam in the frequency range 30 kHz to 1 MHz of $dP/df \sim 10^{-9}$ W/Hz for the DC flux tube connection sequence.

4. CONCLUSIONS

Injection of low-power (1-keV, 50- and 100-mA) electron beams from the space shuttle orbiter produces waves in the ionospheric plasma. During the Spacelab 2 mission wideband wave receiver and PDP filter bank data were obtained at various distances from the electron beam during the free flight of the plasma diagnostics package. During both the DC and the Pulsed flux tube connection sequences the operation of the electron beam produced broadband wave emissions. During the Pulsed flux tube connection narrow-band waves were also produced at the harmonics of the pulsing frequency. The dependence of the wave amplitudes on the frequency of the waves and the distance between the receiver and the beam were analyzed to gain understanding of the production and propagation of these waves and the features observed in the data.

The amplitudes of the narrow-band waves were compared with the predictions of the theory of *Harker and Banks* [1987] and *Neubert and Harker* [1988]. Comparisons of the dependence of predicted and measured wave amplitudes on harmonic number and on distance to the beam show the best agreement for the waves generated through the Cherenkov resonance with wave normals in the central hump of the index surface (s=0, root 2). Comparisons between the predicted amplitudes for the $s = 0$, root 2 solutions and the measured amplitudes show that the measured amplitudes were less than the predicted amplitudes for the odd harmonics but that they agreed to within better than a factor of 30. The most significant difference between the predictions and observations was the presence of measurable waves at the even, "forbidden" frequencies, which is likely to be caused by a partial loss of the spatial coherence of the square-wave modulated beam.

The electromagnetic character of the narrow-band waves was investigated by calculating the expected value of $c\langle B\rangle/\langle E\rangle$ for whistler mode Cherenkov radiation and comparing that with measured values. Both were found to be of order 10, as were values for natural whistlers. An estimate of the Poynting flux was made from fields measured at 22 m and 61 m from the beam. For the fundamental at 1.22 kHz, $|\mathbf{S}|$ was estimated at 10^{-12} W/(m^2 Hz) for a 12-Hz bandwidth.

Broadband electric and magnetic fields were both observed above ambient levels. The electric and the magnetic fields exhibit a similar dependence of amplitude on distance from the beam. These observations indicate the presence of broadband electromagnetic waves in the measured fields. The continuity of the amplitude of both the electric and magnetic wave spectra across the lower hybrid frequency suggests that the electromagnetic component of the broadband waves is produced through the Cherenkov resonance ($s = 0$). Theory predicts that two separate broadband wave fields may be produced through the Cherenkov resonance in the range of observation. Between the lower hybrid frequency and the electron cyclotron frequency, resonance cone emissions are produced, and their propagation properties produce a funnel-shaped emission in this frequency range [*Gurnett et al.*, 1986]. At frequencies below the 30-kHz upper limit of the wideband receiver the broadband resonance cone emissions are entirely confined to the region near the beam. In the VLF range, broadband waves are also observed at larger distances from the beam. Comparison with theory suggests that this is radiation with wave normal vectors in the central hump of the index of refraction surface. This is the same wave mode as for the narrow-band waves. The upper cutoff is due to the inability to satisfy the Cherenkov resonance condition in the central hump above a critical frequency which is ~30 kHz for the DC flux tube connection sequence. All measurements were made within one perpendicular wavelength for the waves in this mode. The observation of waves outside the predicted propagation region is attributed to near fields.

Strong electric fields which are associated with a sheet of low-energy electrons in the beam wake are interpreted as ion acoustic waves [*Frank et al.*, 1989]. These broadband waves have the largest effect in the beam wake but may also contribute to the electric fields observed in zone 3, outside the beam wake.

As well as providing an explanation for many of the features observed in the data this analysis provides an important foundation for future experiments. For example, knowing the wave mode helps in the optimization of experiments in the propagation of electron beam-generated radiation to remote detectors on the ground or on satellites. However, it is also clear that significant gaps remain in our understanding of the production of waves through the interaction of electron beams with space plasmas. Among the most intriguing questions which remain are; (1) What are the electron beam structures which produce the broadband emissions or the narrow-band emissions at the forbidden harmonics and what are the propagation properties of the beam electrons themselves? (2) What is the role of the return currents, spacecraft charging, and electron beam escape in the production of waves? (3) How efficiently is the beam kinetic energy converted to wave energy and what is the total radiated wave power from the beam? (4) Why are the measured ratios of electric and magnetic field com-

ponents different for the broadband and narrow-band emissions? (5) Why are the narrow-band resonance cone emissions predicted by theory not observed? Although we may begin to address some of these questions using the results of observations from the electron beam experiments which have been completed, some require further investigation and some must await future research.

Acknowledgements. The authors would like to thank L. Frank for his valuable contributions. This work was conducted at Stanford University under NASA grant NAGW-225.

The Editor thanks R. W. Fredricks and another referee for their assistance in evaluating this paper.

REFERENCES

Al'pert, Ya. L., *The Near Earth and Interplanetary Plasma*, Cambridge University Press, New York, 1983.

Banks, P. M., W. J. Raitt, R. I. Bush, and P. R. Williamson Results from the vehicle charging and potential experiment on STS-3, *J. Spacecr. Rockets, 24*, 138, 1987.

Bell, T. F., Artificial production of VLF hiss, *J. Geophys. Res., 73*, 13, 1968.

Bilitza, D., International reference ionosphere: Recent developments, *Radio Sci., 21*, 343, 1986.

Bush, R. I., G. D. Reeves, P. M. Banks, T. Neubert, P. R. Williamson, W. J. Raitt, and D. A. Gurnett, Electromagnetic fields from pulsed electron beam experiments in space: Spacelab 2 results, *Geophys. Res. Lett., 14*, 1015, 1987.

Farrell, W. M., D. A. Gurnett, P. M. Banks, R. I. Bush, and W. J. Raitt, An analysis of the whistler-mode radiation from the Spacelab 2 electron beam, *J. Geophys. Res., 93*, 153, 1988.

Frank, L. A., W. R. Paterson, M. Ashour-Abdalla, D. Schriver, W. S. Kurth, D. A. Gurnett, N. Omidi, P. M. Banks, R. I. Bush, and W. J. Raitt, Electron velocity distributions and plasma waves associated with the injection of an electron beam into the ionosphere, *J. Geophys. Res., 94*, 6995, 1989.

Gekelman, W., and R. L. Stenzel, Ion sound turbulence in a magnetoplasma, *Phys. Fluids, 21*, 2014, 1978.

Gurnett, D. A., W. S. Kurth, J. T. Steinberg, P. M. Banks, R. I. Bush, and W. J. Raitt, Whistler-mode radiation from the Spacelab 2 electron beam, *Geophys. Res. Lett., 13*, 225, 1986.

Harker, K. J., and P. M. Banks, Near fields in the vicinity of pulsed electron beams in space, *Planet. Space Sci., 35*, 1, 1987.

Hawkins, J. G., Vehicle charging and return current measurements during electron beam emission experiments from the shuttle orbiter, Ph.D. dissertation, Stanford Univ., Stanford, Calif., 1988.

Myers, N. B., W. J. Raitt, A. B. White, P. M. Banks, B. E. Gilchrist, and S. Sasaki, Vehicle charging effects during electron beam emissions from the CHARGE-2 experiment, *J. Spacecr. Rockets*, in press, 1989.

Neubert, T., and K. J. Harker, Magnetic fields in the vicinity of pulsed electron beams in space, *Planet. Space Sci., 36*, 469, 1988.

Neubert, T., J. G. Hawkins, G. D. Reeves, P. M. Banks, R. I. Bush, P. R. Williamson, D. A. Gurnett, and W. J. Raitt, Pulsed electron beam emissions in space, *J. Geomagn. Geoelectr., 40*, 1221, 1989*a*.

Neubert, T., K. J. Harker, P. M. Banks, G. D. Reeves, and D. A. Gurnett, Waves generated by pulsed electron beams, *Adv. Space Sci.*, in press, 1989*b*.

Okuda, H., and M. Ashour-Abdalla, Ion-acoustic instabilities excited by injection of an electron beam in space, *J. Geophys. Res., 93*, 2011, 1988.

Reeves, G. D., Very low frequency radio waves produced by electron beam injection in space plasmas, Ph.D. dissertation, Stanford Univ., Stanford, Calif., 1989.

Reeves, G. D., P. M. Banks, A. C. Fraser-Smith, T. Neubert, R. I. Bush, D. A. Gurnett, and W. J. Raitt, VLF wave stimulation by pulsed electron beams injected from the space shuttle, *J. Geophys. Res., 93*, 162, 1988*a*.

Reeves, G. D., P. M. Banks, T. Neubert, R. I. Bush, P. R. Williamson, A. C. Fraser-Smith, D. A. Gurnett, and W. J. Raitt, VLF wave emissions by pulsed and dc electron beams in space, 1, Spacelab 2 observations, *J. Geophys. Res., 93*, 14699, 1988*b*.

Shawhan, S. D., G. B Murphy, and J. S. Pickett, Plasma diagnostics package initial assessment of the STS 3 orbiter plasma environment, *J. Spacecr. Rockets, 21*, 387, 1984*a*.

Shawhan, S. D., G. B. Murphy, P. M. Banks, P. R. Williamson, and W. J. Raitt, Wave emissions from dc and modulated electron beams on STS 3, *Radio Sci., 19*, 471, 1984*b*.

Winckler, J. R., The application of artificial electron beams to magnetospheric research, *Rev. Geophys., 18*, 659, 1980.

Winglee, R. M., and P. L. Pritchett, Space-charge effects during the injection of dense electron beams into space plasmas, *J. Geophys. Res., 92*, 6114, 1987.

Winglee, R. M., and W. L. Pritchett, Comparative study of cross-field and field-aligned electron beams in active experiments, *J. Geophys. Res., 93*, 5823, 1988.

P. M. Banks, K. J. Harker, and T. Neubert, STAR Laboratory, Durand 202, Stanford University, Stanford, CA 94305.

D. A. Gurnett, Department of Physics and Astronomy, University of Iowa, Iowa City, IA 52242.

G. D. Reeves, Los Alamos National Laboratory, D-438, Los Alamos, NM 87545.

(Received April 18, 1988;
revised August 28, 1989;
accepted August 30, 1989.)

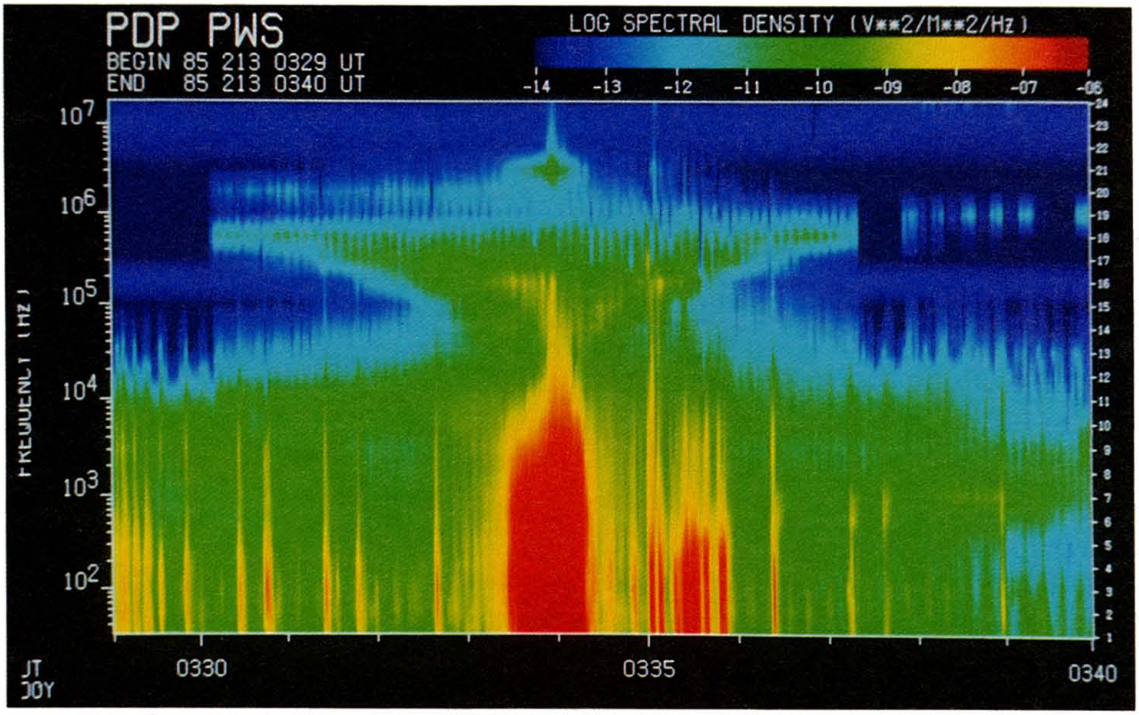

Plate 1 [*Reeves et al.*]. The spectral intensity of waves observed during the DC flux tube connection sequence plotted as a function of frequency and time. The data were obtained using the IMP/Helios and MFR filter banks which had four 10% bandwidth filters per. frequency decade. Among the features observed are the funnel-shaped emissions due to resonance cone propagation, the cutoff of $\mathcal{VLF}$ emissions above 30 kHz, and the dependence on frequency of $\mathcal{VLF}$ emissions observed at various locations with respect to the conjunction field line. Lower-frequency ($f < 1$ kHz) waves are observed at greater distances from the conjunction field line and therefore appear at earlier and later times than higher-frequency ($1 < f < 30$ kHz) waves. See Figure 1 for the location of the PDP for various times.

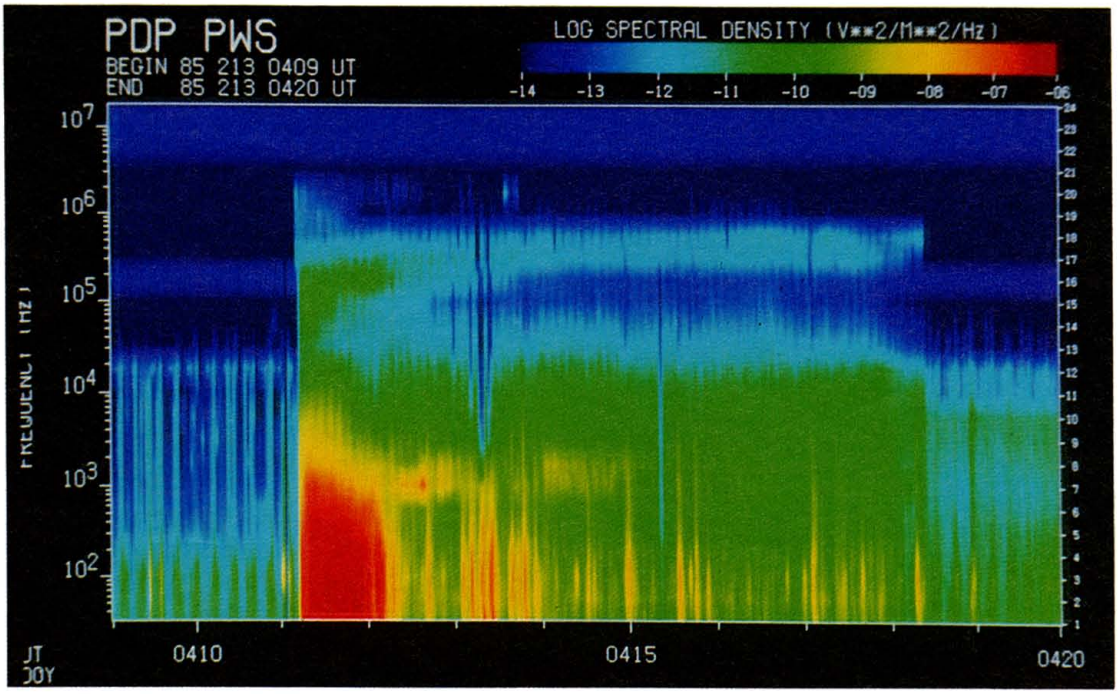

Plate 2 [*Reeves et al.*]. The spectral intensity of waves observed during the Pulsed flux tube connection sequence. The format is the same as for Plate 1.